Nanostructures and defects in nonequilibrium-synthesized filled skutterudite $CeFe_4Sb_{12}$

Juan Zhou, Qing Jie, Lijun Wu, Ivo Dimitrov, and Qiang Li[a)]
Condensed Matter Physics and Materials Science Department, Brookhaven National Laboratory, Upton, New York 11973

Xun Shi
CAS Key Laboratory of Materials for Energy Conversion, Shanghai Institute of Ceramics, Chinese Academy of Sciences, Shanghai 200050, China

(Received 11 December 2010; accepted 22 February 2011)

We studied nanoprecipitates (NPs) and defects in p-type filled skutterudite $CeFe_4Sb_{12}$ prepared by a nonequilibrium melt spinning plus spark plasma sintering method using transmission electron microscopy. NPs with mostly spherical shapes and different sizes (from several nanometers to several tens of nanometers) have been observed. Among these, two types of NPs were most commonly observed, Sb-rich superlattices and $CeSb_2$. The Sb-rich superlattices with a periodicity of about 3.6 nm were induced by the ordering of excessive Sb atoms along the *c*-direction. These NPs typically share coherent interfaces with the surrounding matrix and induce anisotropic strain fields in the matrix. NPs with compositions close to $CeSb_2$, on the other hand, have been shown to be much larger in size (~30 nm) and have orthorhombic structures. Various defects were typically observed on the interfaces between these NPs and the matrix. The strain fields induced by these NPs are less distinct, possibly because part of the strain has been released by defect formation.

I. INTRODUCTION

The efficiency of a thermoelectric (TE) material is measured by the dimensionless figure of merit $ZT = S^2\sigma T/\kappa$, where S, σ, T, and κ stand for the Seebeck coefficient, electrical conductivity, absolute temperature, and thermal conductivity, respectively.[1] The total thermal conductivity, κ, includes two parts: the electrical contribution, κ_e, and the lattice contribution, κ_L, the latter of which can be tuned almost independently of other parameters. Filled skutterudites are typical materials for the phonon glass electron crystal paradigm,[2] and they have been shown to exhibit much lower κ_L than their parent compounds. Filler atoms, such as rare earth,[3,4] alkali,[5] or alkaline earth[6] elements have been utilized to fill the cages of the open-host skutterudite structures to cause localized rattling, superimposed on the collective motions of lattice plane waves, leading to the scattering of heat-carrying acoustic phonons. In addition to filling parent compounds, nanostructuring has been shown to play an important role in reducing the thermal conductivities of a variety of TE materials.[7–9]

Nonequilibrium synthesis techniques such as rapid solidification and fast sintering are known for producing materials with nanostructures. Recently, a nonequilibrium synthesis method combining melt spinning with subsequent spark plasma sintering (SPS) or hot press has been successfully used in the preparation of filled skutterudites[10–12] and several other TE materials.[13–15] Nonequilibrium-synthesized n-type $Yb_{0.2}Co_4Sb_{12+y}$ samples with excess Sb have shown dispersion of nanoscale secondary phase on the grain boundaries.[12] These nanostructures were believed to have reduced κ_L and improved the electrical properties at the same time.

Nonequilibrium synthesis provides a fast and economical way of processing bulk TE materials with superior properties. In this article, we report our combined high-resolution transmission electron microscopy (HRTEM) imaging with chemical composition, lattice mismatch, and strain field analysis of nanoprecipitates (NPs) in the nonequilibrium-synthesized $CeFe_4Sb_{12}$ samples.

II. EXPERIMENTAL PROCEDURE

A. Nonequilibrium synthesis of $CeFe_4Sb_{12}$ polycrystals

High purity element pieces of Ce (99.8%), Fe (99.98%), and Sb (99.9999%) at stoichiometric amounts were loaded into boron nitride tubes, which were then sealed under Ar pressure. The raw materials were molten at about 1450 °C for 30 s in an induction furnace and then cooled down to room temperature in 30 min. The obtained ingot was placed into a quartz tube with a 0.5-mm-diameter nozzle, molten and injected under an Ar pressure of 0.067 MPa onto a copper wheel rotating at a linear speed of 30 m/s. The absolute temperature of the stoichiometric

a)Address all correspondence to this author.
e-mail: qiangli@bnl.gov
DOI: 10.1557/jmr.2011.79

 © Materials Research Society 2011

https://doi.org/10.1557/jmr.2011.79 Published online by Cambridge University Press

mixture was not measured directly, but this was not necessary as it was fully molten before melt spinning.

The melt-spun ribbons were subsequently subjected to SPS to form dense pellets. The final SPS temperature and pressure utilized were 620 °C and 50 MPa, respectively. The samples were heated up to 620 °C in 2 min and then held at this temperature for 3 min. The power was then shut off, and the densified pellet was cooled to 200 °C in 10 min and subsequently cooled down to room temperature.

The phase composition of the sintered bulk samples was examined by a Philips XRG 3100 X-ray diffractometer using Cu K_α radiation ($\lambda = 0.15418$ nm).

B. High-resolution transmission electron microscopy

Samples for transmission electron microscopy (TEM) observation were prepared by a traditional dimpling method. After mechanical polishing and dimpling to a thickness of about 20 μm, the samples were thinned to electron transparency using an ion mill system at low milling angles (6–12°). The specimen stage of the ion mill system was cooled with liquid nitrogen, which helped avoid overheating of local specimen during the milling process to reduce damage to the sample. All TEM samples were ion milled below −90 °C. HRTEM was performed on a JEOL JEM 2100F TEM equipped with a Schottky field emission gun and two exchangeable objective lens pole pieces. The ultrahigh resolution pole piece has a 0.19-nm point-to-point resolution and a ± 20° sample tilt, and the high resolution pole piece has a 0.23-nm point-to-point resolution and a ± 40° sample tilt. It is also equipped with an Oxford energy dispersive X-ray spectrometer (EDS) for chemical analysis.

The local distribution of the strain field around NPs was retrieved using the geometric phase analysis (GPA) software. GPA is capable of generating quantitative deformation and strain maps from standard HRTEM images based on the geometric phase algorithms originally developed by Martin Hytch.[16] The first step was to calculate the Fourier transform of the HRTEM image.[7] Phase images were obtained by centering a small aperture on a strong reflection spot $\boldsymbol{g}$, followed by an inverse Fourier transform. The phase component $P'_g(\boldsymbol{r})$ of the phase image is related to the lattice displacement $\boldsymbol{u(r)}$ by

$$P_g(\boldsymbol{r}) = P'_g(\boldsymbol{r}) - 2\pi \boldsymbol{g}\cdot\boldsymbol{r} = -2\pi \boldsymbol{g}\cdot\boldsymbol{u}(\boldsymbol{r}) \quad ,$$

where $\boldsymbol{g}$ is the reciprocal lattice vector from the undistorted reference lattice. The two-dimensional displacement field can be derived by applying the method to two noncollinear Fourier components, e.g., $\boldsymbol{g_1}$ and $\boldsymbol{g_2}$.

$$P_{g1}(\boldsymbol{r}) = -2\pi \boldsymbol{g_1}\cdot\boldsymbol{u}(\boldsymbol{r}) = -2\pi[\boldsymbol{g_{1x}}\boldsymbol{u_x}(\boldsymbol{r}) + \boldsymbol{g_{1y}}\boldsymbol{u_y}(\boldsymbol{r})] \quad ,$$

$$P_{g2}(\boldsymbol{r}) = -2\pi \boldsymbol{g_2}\cdot\boldsymbol{u}(\boldsymbol{r}) = -2\pi[\boldsymbol{g_{2x}}\boldsymbol{u_x}(\boldsymbol{r}) + \boldsymbol{g_{2y}}\boldsymbol{u_y}(\boldsymbol{r})] \quad ,$$

where $\boldsymbol{g_{1x}}$, $\boldsymbol{g_{1y}}$, $\boldsymbol{g_{2x}}$, and $\boldsymbol{g_{2y}}$ are the x and y components of the $\boldsymbol{g_1}$ and $\boldsymbol{g_2}$ vectors, respectively. $\boldsymbol{u_x(r)}$ and $\boldsymbol{u_y(r)}$ are the x and y components of the displacement field $\boldsymbol{u(r)}$ at the position $\boldsymbol{r} = (\boldsymbol{x}, \boldsymbol{y})$ in the image, respectively. The strain field is then calculated by

$$\varepsilon_{xx} = \partial \boldsymbol{u_x}/\partial \boldsymbol{x},\ \varepsilon_{yy} = \partial \boldsymbol{u_y}/\partial \boldsymbol{y} \quad .$$

III. RESULTS AND DISCUSSION

Strong and sharp reflection peaks were observed in the x-ray diffraction (XRD) patterns of the experimental samples (Fig. 1). The reflection peaks were indexed as the majority of the $CeFe_4Sb_{12}$ phase with trace amount of $FeSb_2$, indicating the complete conversion and crystallization of bulk materials from melt-spun ribbons by the very short-duration SPS process.

The grains of the experimental samples have been reported to vary from several hundred nanometers to around 1 μm.[17] Individual grains containing abundant NPs were readily observed in the samples, as shown in Fig. 2(a). The TEM image in Fig. 2(b) shows the kind of NPs that are most typically observed. They have spherical shapes with coarse fringes. Further HRTEM imaging shows that they are typically coherently embedded in the matrix. The size of this kind of NPs varies from a few nanometers to <20 nm.

EDS analysis suggests that there is no appreciable difference between the sample stoichiometry before and after melt spinning. This shows that off-stoichiometry is not required to produce NPs.

Figure 3(a) is an HRTEM image viewed along the [100] direction, showing two such kind of NPs coherently embedded in the matrix of a single grain. The two NPs are about 15 nm in diameter and show fringes with the spacing being about 3.576 nm. No obvious lattice distortion was observed on the interfaces between the NPs and

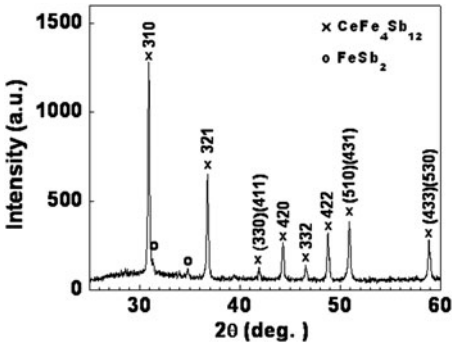


FIG. 1. An x-ray diffraction pattern of $CeFe_4Sb_{12}$ bulk samples synthesized by the nonequilibrium method.

https://doi.org/10.1557/jmr.2011.79 Published online by Cambridge University Press

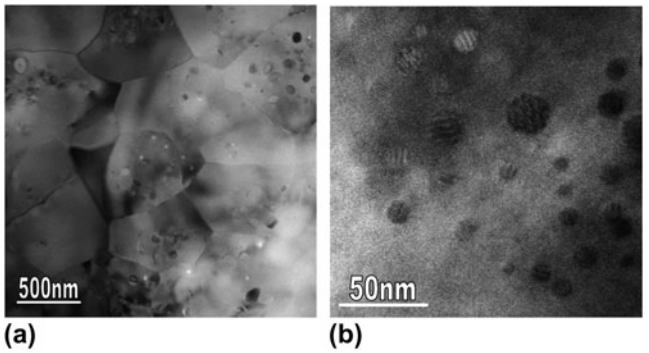


FIG. 2. Transmission electron microscope images at (a) low and (b) high magnifications showing nanometer-sized grains of the nonequilibrium-synthesized $CeFe_4Sb_{12}$ samples containing abundant nanoprecipitates (NPs).

the surrounding matrix. Here, we denote the two NPs as NP-I and NP-II [Fig. 3(a)]. The fast Fourier transform (FFT) diffractograms from the circled matrix area M and the NP area NP-I are shown in Figs. 3(b) and 3(c), respectively. The matrix is confirmed to be the body-centered cubic–filled skutterudite structure. EDS measurements show that the concentration of Sb in the NP-I and NP-II areas is significantly higher than that of the neighboring matrix. NP-I and NP-II areas are determined to be incommensurate superstructures in the lattice in which excessive Sb atoms order along the matrix *c*-direction and induce superlattice reflection spots [Fig. 3(c)]. Figure 3(d) shows the line scan of the 002 peak intensity profile from the matrix (red open circles). Accurate lattice parameters were obtained by fitting the profile using a combination of a Gaussian and a Lorentzian function. The black solid line in Fig. 3(d) is the fitting of

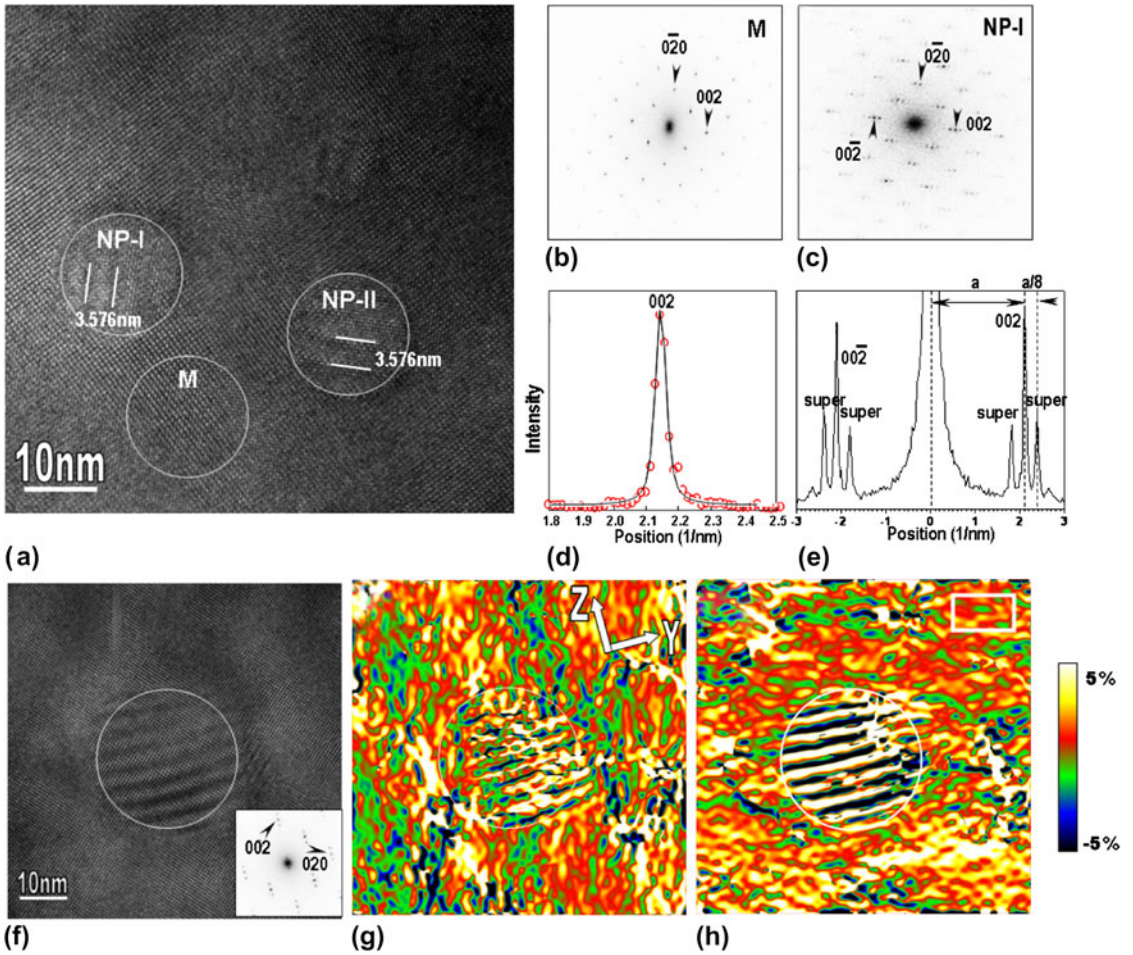


FIG. 3. (a) A high-resolution transmission electron microscope (HRTEM) image of the studied $CeFe_4Sb_{12}$ sample viewed along the [100] zone axis, showing two NPs coherently embedded in the matrix, designated as NP-I and NP-II. The fast Fourier transform (FFT) diffractograms of the circled matrix area M and NP area NP-I in (a) are shown in (b) and (c), respectively. In (c), the presence of superlattice reflections spots is evident. (d) Combined Gaussian and Lorentzian fitting (black solid line) to the 002 peak of the matrix (red open circles). (e) Line scan of intensity profiles from 00−2 peak to 002 peak of the diffractogram of NP-I in (c). (f) An HRTEM image with a NP embedded. FFT diffractogram of the circled NP region is shown in the inset. (g, h) Strain maps of ε_{yy} and ε_{zz}, which were calculated from the HRTEM image shown in (f). The white rectangle in (h) is the reference area. The maps are shown in color for clarity. The circles in the figures outline the NP.

https://doi.org/10.1557/jmr.2011.79 Published online by Cambridge University Press

the 002 matrix peak, from which the lattice parameter of the matrix is determined to be 0.918 ± 0.003 nm. The line scan of the intensity profile from 00−2 peak to 002 peak of the FFT diffractogram [Fig. 3(c)] of NP-I area is shown in Fig. 3(e). The spacing between the main spots and the superlattice spots is measured to be 0.28 nm^{-1}, indicating that the periodicity of the superlattice in NP-I area is about four times larger than that of the matrix. Since the matrix has a cubic structure with equivalent *a*-, *b*-, and *c*-axes, the ordering of Sb atoms can be along the *a*- or *b*-directions of the matrix as well. The periodicity of superlattice in NP-II area is same to that of NP-I area, as marked in Fig. 3(a), except that the ordering of the superlattice in NP-II is along the *b*-direction.

Strain field distribution retrieved by the GPA software is a relative strain map with respect to the reference area. Figure 3(f) shows an HRTEM image of a NP in which the FFT diffractogram from the circled NP area is shown in the inset. Figures 3(g) and 3(h) show the relative strain maps, ε_{yy} and ε_{zz}, retrieved from the HRTEM image in Fig. 2(f) with $\boldsymbol{g_1} = 020$ and $\boldsymbol{g_2} = 002$, and *y*- and *z*-axes pointing to the [010] and [001] directions, respectively. The reference area is marked by a white rectangle in Fig. 3(h). The ε_{yy} map exhibits both positive and negative strains and the ε_{zz} map shows strong positive strains in the matrix. Although the NP has a symmetric (circular) shape, ε_{yy} and ε_{zz} strains around the NP are anisotropic. There are small regions near the NP showing positive values of ε_{xx}, and ε_{zz} is larger on the bottom side than the top side. The anisotropic distribution of the strain field around the NPs with symmetric shapes has also been observed in $AgPb_mSbTe_{m+2}$ (LAST-18) single crystals.[7] One possible explanation is that strain fields are not only caused by the misfit between NPs and the matrix but also by the local fluctuations in composition. The formation of Sb-rich NPs consumes Sb, which naturally induces local compositional fluctuation in the surrounding matrix. It is also possible that the formation of Sb-rich superlattices may be caused by the Ce-filling fraction fluctuation, since a very quick sintering has been used to inhibit grain growth. The alternate

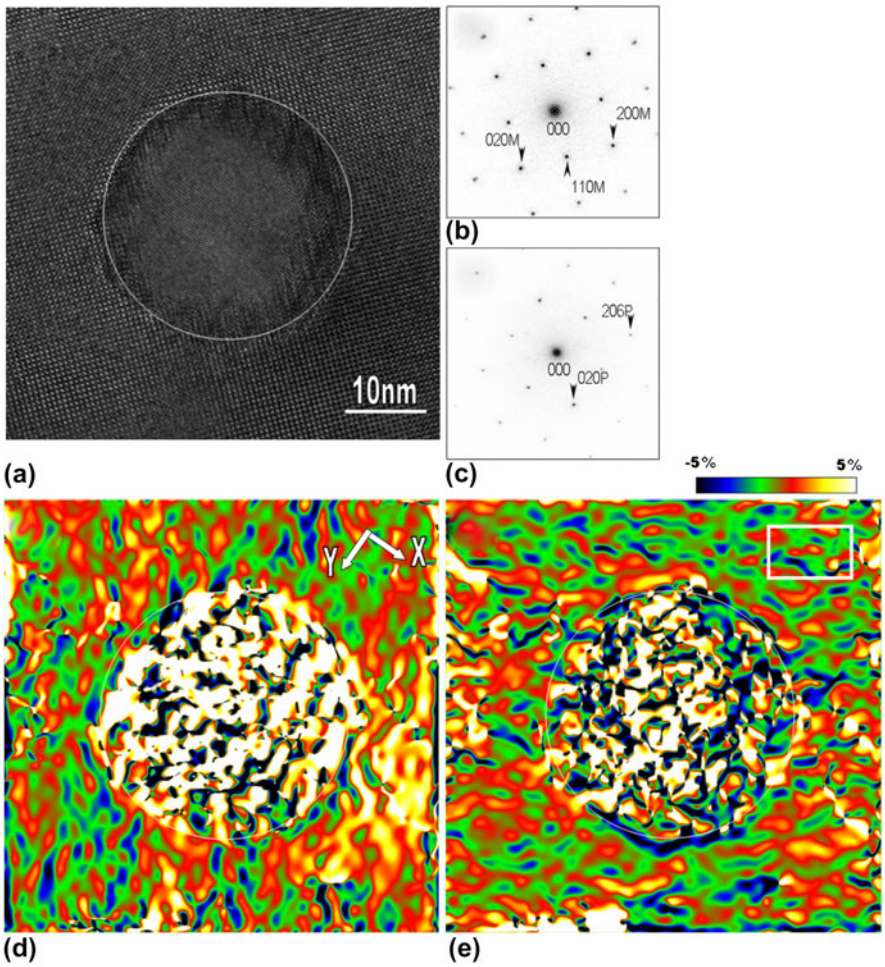


FIG. 4. (a) HRTEM image showing a $CeSb_2$ NP embedded in the matrix of the nonequilibrium-synthesized $CeFe_4Sb_{12}$ sample. Corresponding FFT diffractograms from the matrix and the circled NP areas in (a) are shown in (b) and (c), respectively. Strain maps of (d) ε_{xx} and (e) ε_{yy} are calculated from the HRTEM image in (a). The white rectangle in (e) is the reference area. The circles in the figures outline the NPs.

https://doi.org/10.1557/jmr.2011.79 Published online by Cambridge University Press

contrast inside the NP areas was formed by the modulated superlattice structures.

Figure 4(a) shows the HRTEM image viewed along the [001] matrix direction, showing another typical kind of NPs in the studied $CeFe_4Sb_{12}$ samples. It has a spherical shape and is about 30 nm in diameter. EDS analysis shows that the composition of the NP is close to $CeSb_2$. The FFT diffractograms from the matrix and the circled NP areas are shown in Figs. 4(b) and 4(c), respectively. The NP was indexed to be a $CeSb_2$ orthorhombic structure with lattice parameters of $a = 0.6295(6)$ nm, $b = 0.6124(6)$ nm, and $c = 1.821(2)$ nm. The orientation relationship between the NP and the matrix was determined to be $(010)_{CeSb2}//(110)_{CeFe4Sb12}$ and $(206)_{CeSb2}//(1\text{–}10)_{CeFe4Sb12}$, respectively. A possible $CeSb_2$ phase was not detected from the XRD pattern (Fig. 1) indicating that only trace amounts of it exist in the sample. In Fig. 4(a), lattice distortions and misfit dislocations were frequently observed surrounding the NP, which are possibly formed to compensate the lattice mismatch between the NP and the neighboring matrix.

Figures 4(d) and 4(e) show the relative strain maps ε_{xx} and ε_{yy}, retrieved from the HRTEM image in Fig. 4(a) with $\boldsymbol{g_1} = 200, \boldsymbol{g_2} = 020$, and x- and y-axes pointing to the [100] and [010] directions, respectively. The reference area is marked by a white rectangle in Fig. 4(e). The ε_{xx} map shows positive strain in both the matrix and the NP, which is smaller on the top left than on the bottom right. The ε_{yy} map shows positive strain in the NP and almost no strain in the matrix. The strain maps are also anisotropic, and ε_{yy} shows much less strain than ε_{xx}. The $CeSb_2$ NPs have defects on the interfaces and produce less distinct strains on the matrix when compared to the Sb-rich NPs, which share coherent interfaces with the matrix. The possible reason may be that part of the strain caused by the $CeSb_2$ NP has been released through the formation of dislocations and other defects on the interface.

IV. CONCLUSIONS

NPs in nonequilibrium-synthesized $CeFe_4Sb_{12}$ have been analyzed in detail using quantitative HRTEM. The Sb-rich NPs usually share coherent interfaces with the matrix. Large $CeSb_2$ NPs were observed with lattice distortions and misfit dislocations on the interface with the matrix. The strain fields in the matrix around these spherical NPs have been shown to be anisotropic. Coherent interfaces between NPs and the matrix seem to induce more distinct strain fields than the interfaces with defects. The formation of defects on the interface may have released part of the strains. The high density of additional interfaces and strain fields produced by nanometer-sized grains, NPs, and defects are believed to enhance phonon scattering and result in a significant reduction in κ_L. Currently, ab initio density functional theory and lattice dynamical models are being aimed at modeling the strain formation around the NPs that were observed in the HRTEM imaging of our sample and future inelastic neutron scattering measurements are planned to observe potential effects of nanostructuring on the phonon density of states in a number of filled skutterudites.

ACKNOWLEDGMENTS

We thank Dr. Jihui Yang of Materials and Processes Laboratory, General Motors R&D Center for generous help with sample preparation. We thank the Center for Functional Nanomaterials, Brookhaven National Laboratory for generous support in using its facilities. The work at Brookhaven National Laboratory was primarily supported by the U.S. Department of Energy, Office of Basic Energy Science, Materials Science and Engineering Division, under Contract No. DE-AC02-98CH10886. This research was also partly supported by the Cooperative Research and Development Agreements (CRADA) between Brookhaven National Laboratory (Q. Li) and General Motors Corporation (J.H. Yang).

REFERENCES

1. H.J. Goldsmid: *Thermoelectric Refrigeration*. (Plenum Press, New York, 1964).
2. G.A. Slack: *CRC Handbook of Thermoelectrics*, edited by D.M. Rowe (CRC Press, Boca Raton, FL, 1995).
3. D.T. Morelli and G.P. Meisner: Low temperature properties of the filled skutterudite $CeFe_4Sb_{12}$. *J. Appl. Phys.* **77**, 3777 (1995).
4. G.S. Nolas, G.A. Slack, D.T. Morelli, T.M. Tritt, and A.C. Ehrlich: The effect of rare-earth filling on the lattice thermal conductivity of skutterudites. *J. Appl. Phys.* **79**, 4002 (1996).
5. Y.Z. Pei, L.D. Chen, W. Zhang, X. Shi, S.Q. Bai, X.Y. Zhao, Z.G. Mei, and X.Y. Li: Synthesis and thermoelectric properties of $K_yCo_4Sb_{12}$. *Appl. Phys. Lett.* **89**, 221107 (2006).
6. L.D. Chen, T. Kawahara, X.F. Tang, T.H.T. Goto, I.J.S. Dyck, W. Chen, and C. Uher: Anomalous barium filling fraction and n-type thermoelectric performance of $Ba_yCo_4Sb_{12}$. *J. Appl. Phys.* **90**, 1864 (2001).
7. L.J. Wu, J.C. Zheng, J. Zhou, Q. Li, J.H. Yang, and Y.M. Zhu: Nanostructures and defects in thermoelectric $AgPb_{18}SbTe_{20}$ investigated by quantitative high resolution transmission electron microscopy. *J. Appl. Phys.* **105**, 094317 (2009).
8. K.F. Hsu, S. Loo, F. Guo, W. Chen, J.S. Dyck, C. Uher, T. Hogan, E.K. Polychroniadis, and M.G. Kanatzidis: Cubic $AgPb_mSbTe_{2+m}$: Bulk thermoelectric materials with high figure of merit. *Science* **303**, 818 (2004).
9. B. Poudel, Q. Hao, Y. Ma, Y.C. Lan, A. Minnich, B. Yu, X. Yan, D.Z. Wang, A. Muto, D. Vashaee, X.Y. Chen, J.M. Liu, M.S. Dresselhaus, G. Chen, and Z.F. Ren: High-thermoelectric performance of nanostructured bismuth antimony telluride bulk alloys. *Science* **320**, 634 (2008).
10. Q. Li, Z.W. Lin, and J. Zhou: Thermoelectric materials with potential high power factors for electricity generation. *J. Electron. Mater.* **38**, 1268 (2009).
11. Q. Jie, J. Zhou, I.K. Dimitrov, C.P. Li, C. Uher, H. Wang, W. Porter, and Q. Li: Thermoelectric properties of non-equilibrium synthesized $Ce_{0.9}Fe_3CoSb_{12}$ filled skutterudites, in *Thermoelectric Materials–Growth, Properties, Novel Characterization Methods, and Applications*, edited by H.L. Tuller, J.D. Baniecki, G.J. Snyder,

https://doi.org/10.1557/jmr.2011.79 Published online by Cambridge University Press

and J.A. Malen (Mater. Res. Soc. Symp. Proc. **1267**, Warrendale, PA, 2010), DD03-03.
12. H. Li, X.F. Tang, X.L. Su, and Q.J. Zhang: Preparation and thermoelectric properties of high-performance Sb additional $Yb_{0.2}CoSb_{12+y}$ bulk materials with nanostructures. *Appl. Phys. Lett.* **92**, 202114(1–3) (2008).
13. X.F. Tang, W.J. Xie, H. Li, W.Y. Zhao, and Q.J. Zhang: Preparation and thermoelectric transport properties of high-performance p-type Bi_2Te_3 with layered nanostructure. *Appl. Phys. Lett.* **90**, 012102(1–3) (2007).
14. Y. Chen, T.J. Zhu, S.H. Yang, S.N. Zhang, W. Miao, and X.B. Zhao: High-performance $(Ag_xSbTe_{x/2+1.5})_{15}(GeTe)_{85}$ thermoelectric materials prepared by melt spinning. *J. Electron. Mater.* **39**, 1719 (2010).
15. C. Yu, T.J. Zhu, K. Xiao, J.J. Shen, S.H. Yang, and X.B. Zhao: Reduced grain size and improved thermoelectric properties of melt spun (Hf, Zr)NiSn half-Heusler alloys. *J. Electron. Mater.* **39**, 2008 (2010).
16. M.J. Hÿtch, E. Snoeck, and R. Kilaas: Quantitative measurement of displacement and strain fields from HREM micrographs. *Ultramicroscopy* **74**, 131 (1998).
17. J. Zhou, Q. Jie, and Q. Li: Microstructure investigation of nonequilibrium synthesized filled skutterudite $CeFe_4Sb_{12}$, in *Thermoelectric Materials–Growth, Properties, Novel Characterization Methods, and Applications*, edited by H.L. Tuller, J.D. Baniecki, G.J. Snyder, and J.A. Malen (Mater. Res. Soc. Symp. Proc. **1267**, Warrendale, PA, 2010), DD05-25.

https://doi.org/10.1557/jmr.2011.79 Published online by Cambridge University Press